

Triple-layer coatings prepared by magnetron sputtering as replacement of indium-tin oxide films for photovoltaic applications

Stella Van Eek^{1,*}, Xia Yan², Weimin Li², Sascha Kreher¹, and Selvaraj Venkataraj²

¹*FHR Anlagenbau GmbH, 01458 Ottendorf-Okrilla, Germany*

²*Solar Energy Research Institute of Singapore, National University of Singapore, 117574 Singapore*

*E-mail: vaneek@fhr.de

Indium-tin oxide (ITO) films are used as transparent conductive oxides (TCO) for optoelectronic applications. There is an actual need driven by the high cost of this coating, of replacing ITO with an alternative TCO. In this work the structure Al-doped ZnO (AZO) AZO/Ag/AZO is characterized as a candidate for replacing ITO films. The samples were prepared using different Ag thicknesses. The structure of the films was characterized using Rutherford backscattering analysis, X Rays diffraction, TEM, SEM and AFM.

The AZO/Ag/AZO structure allows a low sheet resistance of around 10 Ω /sq and a visible transmission above 80% achieved with an overall thickness of ~110 nm. The optimization of front AZO thickness helps to reduce reflection via destructive interferences. The adhesion strength of the stacks can be improved by modifying top AZO deposition conditions. The annealing studies confirm good thermal stabilities of the fabricated sandwich structure.

1. Introduction

Transparent conductive oxides (TCOs) belong to a certain class of thin-film materials that can simultaneously exhibit a high optical transparency and a low electrical resistivity. Owing to their unique optoelectronic properties, TCOs have been widely used in various photoelectric devices, such as flat displays, touch panels, and photovoltaic solar cells.^{1, 2)} Conventional TCO materials consist of three types of metal oxide semiconductor: tin-doped indium oxide (ITO), tin oxide (e.g., doped with fluorine, SnO₂:F), and impurity-doped zinc oxide (e.g., doped with a group III element). Among these TCO materials, ITO is currently the market-dominant TCO owing to its excellent electrical and optical properties, as well as fabrication maturity.³⁾ However, the ITO film is known to suffer from a thermal stability issue and comprised of the rare and expensive indium element.⁴⁾ Therefore, an alternative novel transparent conducting coating must be developed to replace or reduce the use of ITO.⁵⁾

Under such a circumstance, the TCO/metal/TCO-based multilayer structure has been extensively investigated as one of the most promising candidates that can be used to replace ITO.⁶⁾ Within the multilayer structure, a very thin metal layer (e.g., Ag, Cu, or Al) was embedded between the two TCO layers to provide a higher electronic conductance.⁷⁾ Silver (Ag) is the first-choice material because, in bulk, it has a very low resistivity (approximately $2 \times 10^{-6} \Omega\text{cm}$), is not easily oxidised, and shows good visible transmittance for very small thicknesses.⁸⁾ Considering the typical TCO resistivity above $10^{-4} \Omega\text{cm}$, the overall sheet resistance is mainly determined by the metal film.⁹⁾ With regard to optical transparency, film transmission is controlled by tuning the constructive and destructive interferences to suppress the visible reflection and thus achieve a selective transparent effect for the multilayer structure.^{10, 11)} However, it should also be noted that the simultaneous optimisation of conductivity and transparency while retaining good adhesion on the glass or flexible polymer substrate presents a considerable challenge in film deposition.¹¹⁾

To date, various TCO/metal/TCO structures have been studied with analogous performance achieved.¹²⁾ However, the ITO film is still the most commonly used TCO layer in this sandwich structure (with a thickness of ~50 nm or below). With a typical Ag layer

thickness varying from 5 to 15 nm, the ITO/Ag/ITO structures on glass substrates generally show good transmission (around 80%) with the corresponding R_{sh} from 15 to 4.2 Ω/sq .¹³⁻¹⁸⁾ In this work, aluminium-doped zinc oxide (AZO) was chosen to completely eliminate the use of indium. In the first part, several AZO/Ag/AZO multilayer coatings were grown on 3-mm-thick soda-lime glass (SLG) substrates by magnetron sputtering. Three different Ag layer thicknesses (approximately 10, 13, and 16 nm) were studied while keeping the AZO thickness constant at 50 nm. In the second part, the top AZO layer thickness was varied from 20 to 100 nm to investigate the effect of the upper TCO layer. Thirdly, the AZO (50 nm)/Ag (10 nm)/AZO (50 nm) structure was selected as the representative sample to evaluate the thermal stability and adhesion of this multilayer TCO structure.

2. Experimental methods

2.1. Sample preparation

In this work, thin-film depositions were performed within an in-line multichamber sputter machine (FHR Anlagenbau Line540), which has one dedicated process chamber for TCO/dielectric thin-film deposition with substrate heating up to 400 °C and another one for metal layer deposition.¹⁹⁻²³⁾ This tool is capable of depositing homogeneous layers on large-area substrates and processing maximum-A3 (30 × 40 cm²)-size glass sheets. AZO films were deposited by pulsed DC magnetron sputtering from dual cylindrical rotatable ceramic ZnO:Al₂O₃ targets (98:2 wt%), while Ag films were deposited by DC magnetron sputtering from planar metallic targets. During deposition, each glass sheet is vertically attached (i.e., portrait format) to a moving carrier and oscillates in front of sputter cathodes for a predefined number of passes, which enable us to adjust the layer thickness. The oscillation speed/range can also be fine-tuned to improve the lateral uniformity of thin-film coatings.

Sputtering deposition was entirely performed in a pure Ar atmosphere while maintaining the chamber pressure constant at around 3×10^{-3} mbar. AZO layers were processed at a substrate temperature of ~200 °C, while a Ag film was deposited at room temperature (RT). During the bottom AZO deposition, the substrate was preheated to the defined temperature. In contrast, the top AZO layer was deposited immediately, reaching the vacuum chamber

with no preheating, in order to minimise the thermal effects. The detailed deposition conditions for each layer are summarised in Table I.

2.2. Characterisation

The optical properties of the multilayer structure were measured using a double-beam UV/vis/NIR spectrophotometer equipped with an integrating sphere (Agilent, Cary 7000). Both the spectral reflectance (R) and transmittance (T) in air were recorded from 300 to 1200 nm. Taking the initial light intensity as unity, the absorbance (A) of the measured film can be calculated by subtracting the total transmittance and reflectance, as given by

$$A = 1 - T - R . \quad (1)$$

The electrical performance of the films is represented by the sheet resistance (R_{sh}), which was measured using the four-point probe method (AIT CMT-SERIES) and also by a Hall measurement system (LakeShore HMS8404) in the van der Pauw configuration. The Hall measurement system was operated in the DC mode with a magnetic field of 1.7 T perpendicular to the sample surface. For this multilayer structure (e.g., AZO/Ag/AZO), R_{sh} can be expressed as a function of the resistance of layers coupled in parallel, as given by

$$1/R_{sh} = 1/R_{AZO-bot} + 1/R_{Ag} + 1/R_{AZO-top} . \quad (2)$$

Film resistivity was calculated based on the obtained mobility and concentration via

$$\rho = 1/ne\mu_e , \quad (3)$$

where ρ is the overall film resistivity, n is the effective carrier concentration, e is the elementary charge, and μ_e is the effective carrier mobility of the sandwich structure.

The structure of the film was characterised using an X-ray diffractometer (XRD; Bruker D8 diffractometer) with a Cu K_α radiation source ($\lambda = 1.5406 \text{ \AA}$). The samples were step-scanned from 30 to 46° in steps of 0.006°. The crystallite size was calculated from the full width at half maximum (FWHM) of XRD spectra via the Scherrer equation²⁴⁾

$$D = K\lambda/B\cos\theta_B = 0.9 \times 0.15406 / B\cos\theta_B, \quad (4)$$

where D is the crystallite size, K is the shape factor (with a typical value of around 0.9), λ is the X-ray wavelength, B is the line breadth of FWHM in radians, and θ_B is the Bragg angle in degrees.

Both scanning electron microscopy (SEM; Carl Zeiss Auriga-39-35) and atomic force microscopy (AFM; Veeco NanoScope D3100) were employed to record the surface morphology of the layer stacks. The AFM images were taken in the central region of each sample with a scan size of $1 \times 1 \mu\text{m}^2$ (512×512 data points) in the tapping mode at a rate of 0.5 Hz. The surface roughness of the thin-film samples was represented by the root-mean-square (RMS) roughness derived from AFM results. The layer thickness was confirmed by both transmission electron microscopy (TEM; Tecnai TF-20) cross-sectional observation and Rutherford backscattering spectrometry (RBS) measurement. The RBS experimental results were fitted by SIMNRA software analysis.

3. Results and discussion

3.1 Effects of Ag interlayer thickness

The Ag interlayer thickness is a crucial factor that determines both the optical transparency and electrical conductance of the AZO/Ag/AZO structure. A thin and continuous metal film may be transparent in the visible spectral range with good electrical conduction, but below a critical film thickness, both the electrical resistivity and the optical absorption rapidly increase.²⁵⁾ This is due to a transition from a continuous film to one composed of distinct islands of metal atoms (aggregated state) with properties that differ considerably from those of the bulk metal.^{25, 26)} Therefore, in this work, the Ag thickness was varied from 10 to 16 nm to study its effects on stack properties.

The Ag interlayer thickness was confirmed from the results of cross-sectional TEM observation (see Fig. 1) and RBS analysis (see Fig. 2). In the sputtered AZO film, some nanocrystalline structures are clearly observed. Figure 2 shows a comparison of the RBS spectra between AZO/Ag/AZO and single-layer AZO structures. The peak at 1.68 MeV is

due to the backscattering from the Ag atoms, while the other two peaks at 1.50 and 1.55 MeV are related to the backscattering caused by the Zn atoms in the top and bottom AZO layers, respectively.

The electrical properties of the three sandwich structures are summarised in Table II. Note that the electrical conductance of the multilayer stacks is primarily contributed by the thin but very conductive Ag interlayer and that the AZO films suffer from a reduced carrier mobility ($4.9 \text{ cm}^2\text{V}^{-1}\text{s}^{-1}$ in this work) for a very small layer thickness.^{21, 27, 28)} The as-deposited single-layer AZO film (50 nm) shows an R_{sh} of $\sim 1700 \text{ }\Omega/\text{sq}$ with a resistivity of $\sim 8 \times 10^{-3} \text{ }\Omega\text{cm}$. The R_{sh} of the AZO/Ag/AZO structure significantly decreases from 10.9 to $3.4 \text{ }\Omega/\text{sq}$ as the Ag thickness increases from 10 to 16 nm. The main enhancement originates from the increment in effective carrier concentration, from 5.3×10^{21} to $1.2 \times 10^{22} \text{ cm}^{-3}$. The effective mobility also becomes slightly improved from 10.3 to $12.3 \text{ cm}^2\text{V}^{-1}\text{s}^{-1}$.

For common semiconductor materials, the transport of electrons is limited by many types of scattering, including phonon scattering (lattice vibration), surface/interface scattering, grain boundary scattering, and ionised impurity scattering. The scattering caused by ionised impurity is dominant in TCO films and decreases continuously as the carrier concentration increases.^{29, 30)} In contrast, in the sandwich structure, the mobility is found to improve at a higher carrier concentration. Han et al. suggested that interface scattering (i.e., scattering in the AZO/Ag and Ag/AZO interface regions) is the key factor in this observed behaviour.²⁶⁾ The sample with a 10 nm Ag interlayer is not a smooth closed layer. Increasing the Ag thickness reduces the interface; therefore, the mobility increases continuously with Ag thickness up to 13 nm where this effect saturates and the Ag layer is then closed. Therefore, interface scattering explains the mobility behaviour better than other scattering mechanisms.

Figure 3 shows a comparison of the spectral variations between the AZO/Ag/AZO multilayer structures with different Ag thicknesses and the single-layer AZO film (50 nm) as the reference sample. The AZO film shows good transparency above 80% together with little absorption, starting from 500 nm to the infrared region. For the AZO/Ag/AZO stacks,

the highest transmission occurs at a wavelength of around 520 nm in all these three samples. As the Ag thickness increases from 10 to 13 and 16 nm, the highest transmission slightly decreases from 81.9 to 80.2 and 74.8% respectively. For both display and certain thin-film solar cell (e.g., fullerene-polymer and wide-bandgap perovskite-based) applications, the main range of interest lies in the visible regime.³¹⁻³³⁾ The stacks with a 10 nm Ag interlayer still show good transmission above 70% at a wavelength of 800 nm, which satisfies the optical needs for these applications. The near-infrared (NIR) range is directly associated with free carrier absorption, and thus the transmittance drops significantly. In the sample with a Ag thickness of 16 nm, despite a very high conductance (ρ of $\sim 4 \times 10^{-5} \Omega\text{cm}$), substantial degradation of optical transparency occurs (less than 40% transmission and $\sim 20\%$ absorption at 800 nm). Hence, it can be concluded that the stack with a 16 nm Ag layer is no longer well suited for application to these thin-film solar cells based on wide-bandgap (e.g., $\sim 1.6\text{--}1.8$ eV) organic and perovskite materials.

The crystalline structure of the multilayer films is revealed by the XRD patterns shown in Fig. 4. The sharp primary peak at $\sim 34.4^\circ$ corresponds to the ZnO $\langle 002 \rangle$ orientation and confirms that the AZO films crystallise in a hexagonal wurtzite structure. The Ag (111) peak (centred at $\sim 38.3^\circ$) intensity gradually increases as the Ag thickness increases from 10 to 16 nm. At the same time, the AZO peak intensity and calculated crystallite size (~ 20 nm) remain relatively the same. This observation indicates that the embedded Ag interlayer does not affect the c -axis growth of AZO columnar grains.

The SEM micrographs and AFM images shown in Fig. 5 reveal the smooth surface morphologies of the AZO/Ag/AZO structures. It is observed that the surface tends to be slightly rougher (i.e., RMS increases from 2.34 to 3.46 nm) as the Ag thickness increases from 10 to 16 nm, and the overall surface roughness still remains to be small. In this case, the combination of high visible transparency, low resistance, and ultrasmooth surface makes this multilayer structure suitable for touch panel and other display applications. In addition, this smooth planar surface is also ideal for application to organic fullerene-polymer-based and perovskite-type solar cells, which helps to prevent/suppress

the formation of pinholes during the absorber deposition process (e.g., spin-on coating technique).

3.2 Effects of AZO top layer thickness

The AZO top layer thickness was varied to optimise the transparency of the sandwich structure via tuning interference fringes. In total, six samples were prepared by increasing the AZO top layer thickness from 20 to 35, 50, 65, 80 and 100 nm. To reduce the interlayer nonuniformity, the oscillation speed during Ag deposition was reduced from 60 to 40 mm/s, while the sputtering power was reduced from 0.6 to 0.5 kW in the experiments in Sects. 3.2–3.4.

The trend in electrical properties is straightforward (see Fig. 6). In the TCO/metal/TCO structure, electrons can be injected from metal layer to TCO, significantly increasing the effective carrier concentration. As the AZO top layer thickness increases from 20 to 100 nm, the Ag interlayer becomes less dominant in the structure. Thus, the resultant carrier concentration decreases from 1.2×10^{22} to $5.5 \times 10^{21} \text{ cm}^{-3}$, while the film resistivity nearly doubles (from 6.3×10^{-5} to $1.2 \times 10^{-4} \text{ }\Omega\text{cm}$). Since the mobility is limited by interface scattering, the effective value fluctuates around $9.5 \pm 0.6 \text{ cm}^2\text{V}^{-1}\text{s}^{-1}$ as the AZO top layer thickness varies. In contrast, the single-layer AZO film ($\sim 50 \text{ nm}$) tends to have a mobility of only $\sim 4.9 \text{ cm}^2\text{V}^{-1}\text{s}^{-1}$ with a carrier concentration of $1.5 \times 10^{20} \text{ cm}^{-3}$, producing a resistivity of nearly $10^{-2} \text{ }\Omega\text{cm}$ (see Table II), which is several orders of magnitude higher than that of the AZO/Ag/AZO multilayer structures.

The optical spectra were compared in Fig. 7. It is clearly shown that the front reflection greatly depends on the AZO top layer thickness. For photovoltaic device applications, a reduced front reflection at around 600 nm is desired, since the light intensity peaks at a particular wavelength. For the AZO/Ag/AZO (20 nm) sample, the lowest reflection ($\sim 6\%$) occurs at a wavelength of 300 nm, with no fringes observed. A destructive interference starts to occur in the AZO/Ag/AZO (35 nm) sample with the lowest reflection of 5.1% at 500 nm, which gradually shifts to the ideal 600 nm ($\sim 6.3\%$) for the AZO/Ag/AZO (50 nm) sample. Further increasing the AZO top layer thickness to 65 and 80 nm pushes the lowest

reflection point towards the NIR region. For the AZO/Ag/AZO (100 nm) sample, an undesired maximal reflection point (~30%) occurs at 600 nm owing to constructive interferences. As a result, the AZO/Ag/AZO (50 nm) sample produces the highest visible transmission (above 80% at ~500–600 nm) among the samples investigated. Another interesting point is their similar absorption in the long-wavelength range (e.g., ~22% at 1200 nm), which confirms that the main absorption loss is caused by the Ag interlayer. Note that the single-layer AZO film absorbs less than 8% of light throughout the NIR region [see Fig. 3(c)].

3.3 Adhesion improvement of AZO/Ag/AZO structure

The adhesion of the AZO/Ag/AZO multilayer films to the glass substrates was examined by the standard adhesive Scotch tape test,³⁴⁾ which is widely used for testing the stability of thin-film coatings. Figure 8 shows the photographs of the three samples analysed after the tape test. As can be seen in Fig. 8, the film deposited using pure Ar gas was completely delaminated during the tape test, indicating a low peel-off strength, which would make the stack design unsuitable for practical applications, because the subsequent layer deposition (e.g., solar cell deposition) on this stack design would build enormous stress, which would lead to peel-off and delamination issues. Hence, it is necessary to improve the peel-off strength (adhesion) of the stack design, which can be achieved by process fine tuning. When part of the deposition gas Ar was replaced with a diluted Ar + O₂ (1%) gas mixture (flow rate: 70 sccm), the partial removal of Ag and AZO was observed (see Fig 8). When the diluted Ar + O₂ (1%) gas flow rate was increased further to 100 sccm, the adhesion strength of the stack improved significantly and no delamination occurred during the tape test. The poor adhesion of the films deposited at a low O₂ partial pressure can be attributed to the accumulated layer stress during multilayer growth, as confirmed by XRD analysis in Fig. 9. A reduction in this residual stress in the coating is important to prevent these thin-films from peeling off the substrates.

3.4 Thermal stability analysis of AZO/Ag/AZO structure

Certain photoelectric applications, such as thin-film solar cells, require stable TCO films at an elevated temperature during device fabrication. For example, fullerene-polymer-based

bulk heterojunction (BHJ) solar cells require a thermal annealing treatment (e.g., ~100–200 °C) to activate their highest efficiency.³⁵⁻³⁷⁾ Similarly, the common perovskite solar cell fabrication also requires heating.³⁸⁻⁴⁰⁾ Thus, to understand the thermal effects on the fabricated sandwich structure, the AZO (50 nm)/Ag (10 nm)/AZO (50 nm) sample was selected as the representative for annealing studies. All the samples were cut from the same A3-size coated glass substrate. Two sets of experiments were carried out with either 5 or 10 min annealing under vacuum conditions (pressure < 10⁻⁶ mbar). The heater temperature was gradually increased from 100 to 200, 250, 300, and 350 °C. The actual substrate temperature of the sample was approximately half of the heater temperature.

Figure 10 shows the variations in carrier concentration, mobility, and resultant film resistivity as a function of annealing temperature. The overall resistivity tends to decrease by ~5–10% after the thermal treatment. In terms of mobility, the as-deposited sample gives an effective value of 8.2 cm²V⁻¹s⁻¹, which reaches ~10.5 cm²V⁻¹s⁻¹ after 200 °C annealing for either 5 or 10 min, and then slightly decreases by ~1 cm²V⁻¹s⁻¹ as the temperature further increases. In contrast, the carrier concentration barely changes and fluctuates at around 8×10²¹ cm⁻³. In addition, the spectral variations are also negligible (figure not shown here). These observed differences may be associated with the lateral inhomogeneities attributed to the sample preparation process.

4. Conclusions

In this work, different multilayer sandwich structures of TCO/metal/TCO have been examined and developed as a promising transparent conductive film with a low resistance, suitable for various applications. An R_{sh} as low as 3.3 Ω/sq with high visible transmission was achieved in the AZO (50 nm)/Ag (16 nm)/ AZO (50 nm) sample. The thickness optimisation of the AZO top layer helps to suppress front reflection by tuning fringe patterns. The 50-nm-thick AZO top layer produces the lowest reflection and thus the highest transmission throughout the visible range (e.g., above 80% at 500–600 nm). The modification of the AZO top layer deposition conditions helps to improve the peel-off strength of the stack, which is necessary for the practical application of the stack design. The annealing studies of AZO (50 nm)/Ag (10 nm)/AZO (50 nm) films confirm good thermal

stabilities of the fabricated structures up to 10 min at a heater temperature of 350 °C. The combination of a high visible transmission, a low electrical resistance, a smooth surface, and good thermal stability makes this AZO/Ag/AZO sandwich structure an ideal candidate for display and organic thin-film solar cell applications.

Acknowledgments

The Solar Energy Research Institute of Singapore (SERIS) is sponsored by the National University of Singapore (NUS) and the National Research Foundation (NRF) of Singapore through the Singapore Economic Development Board (EDB). This work was sponsored by the Advanced TCOs Project in collaboration with FHR Anlagenbau GmbH, Germany. Special thanks to Professor Thomas Osipowicz and Dr. Saumitra K Vajandar from the Centre for Ion Beam Applications (CIBA), NUS for assisting us in the RBS measurement and analysis.

References

- 1) D. S. Ginley and C. Bright, *MRS Bull.* **25**, 15 (2000).
- 2) R. G. Gordon, *MRS Bull.* **25**, 52 (2000).
- 3) K. Ellmer, *Nat. Photonics* **6**, 809 (2012).
- 4) J. Ho Kim, Y.-J. Moon, S.-K. Kim, Y.-Z. Yoo, and T.-Y. Seong, *Ceram. Int.* **41**, 14805 (2015).
- 5) A. Kumar and C. Zhou, *ACS Nano* **4**, 11 (2010).
- 6) M. Theuring, M. Vehse, K. von Maydell, and C. Agert, *Thin Solid Films* **558**, 294 (2014).
- 7) S. Boscarino, I. Crupi, S. Mirabella, F. Simone, and A. Terrasi, *Appl. Phys. A* **116**, 1287 (2014).
- 8) I. Crupi, S. Boscarino, V. Strano, S. Mirabella, F. Simone, and A. Terrasi, *Thin Solid Films* **520**, 4432 (2012).
- 9) M. Tadatsugu, *Semicond. Sci. Technol.* **20**, S35 (2005).
- 10) D. R. Sahu and J.-L. Huang, *Mater. Sci. Eng. B* **130**, 295 (2006).
- 11) D. R. Sahu, S.-Y. Lin, and J.-L. Huang, *Thin Solid Films* **516**, 4728 (2008).
- 12) C. Guillén and J. Herrero, *Thin Solid Films* **520**, 1 (2011).
- 13) M. Chakaroun, B. Lucas, B. Ratier, C. Defranoux, J. P. Piel, and M. Aldissi, *Thin Solid Films* **518**, 1250 (2009).
- 14) C. Guillén and J. Herrero, *Opt. Commun.* **282**, 574 (2009).
- 15) Y.-S. Park, H.-K. Park, J.-A. Jeong, H.-K. Kim, K.-H. Choi, S.-I. Na, and D.-Y. Kim, *J. Electrochem. Soc.* **156**, H588 (2009).
- 16) S. Masato, H. Masatoshi, K. Susumu, and S. Hiroyasu, *Jpn. J. Appl. Phys.* **40**, 3332 (2001).
- 17) A. Klöppel, W. Kriegseis, B. K. Meyer, A. Scharmann, C. Daube, J. Stollenwerk, and J. Trube, *Thin Solid Films* **365**, 139 (2000).
- 18) J. Lewis, S. Grego, B. Chalamala, E. Vick, and D. Temple, *Appl. Phys. Lett.* **85**, 3450 (2004).
- 19) W. Li, X. Yan, A. G. Aberle, and S. Venkataraj, *Int. J. Photoenergy* **2016**, 2124087 (2016).

- 20) W. Li, X. Yan, A. G. Aberle, and S. Venkataraj, *Jpn. J. Appl. Phys.* **54**, 08KC14 (2015).
- 21) X. Yan, W. Li, A. G. Aberle, and S. Venkataraj, *Vacuum* **123**, 151 (2016).
- 22) X. Yan, W. Li, A. G. Aberle, and S. Venkataraj, *J. Mater. Sci: Mater. Electron.* **26**, 7049 (2015).
- 23) X. Yan, S. Venkataraj, and A. G. Aberle, *Int. J. Photoenergy* **2015**, 548984 (2015).
- 24) B. D. Cullity and S. R. Stock: *Elements of X-ray Diffraction*, (Prentice Hall, Upper Saddle River, N J, (2001) 3rd ed.
- 25) K. Seal, M. A. Nelson, Z. C. Ying, D. A. Genov, A. K. Sarychev, and V. M. Shalaev, *Phys. Rev. B* **67**, 035318 (2003).
- 26) H. Han, N. D. Theodore, and T. L. Alford, *J. Appl. Phys.* **103**, 013708 (2008).
- 27) C. Guillén and J. Herrero, *Vacuum* **84**, 924 (2010).
- 28) S.-S. Lin and J.-L. Huang, *Surf. Coatings Technol.* **185**, 222 (2004).
- 29) K. Ellmer and R. Mientus, *Thin Solid Films* **516**, 4620 (2008).
- 30) K. Ellmer and R. Mientus, *Thin Solid Films* **516**, 5829 (2008).
- 31) Z. He, B. Xiao, F. Liu, H. Wu, Y. Yang, S. Xiao, C. Wang, T. P. Russell, and Y. Cao, *Nat. Photonics* **9**, 174 (2015).
- 32) L. J. A. Koster, V. D. Mihailetschi, and P. W. M. Blom, *Appl. Phys. Lett.* **88**, 093511 (2006).
- 33) P.-W. Liang, C.-C. Chueh, X.-K. Xin, F. Zuo, S. T. Williams, C.-Y. Liao, and A. K. Y. Jen, *Adv. Energy Mater.* **5**, 1400960 (2015).
- 34) H. Khatri and S. Marsillac, *J. Phys.: Condens. Matter* **20**, 055206 (2008).
- 35) O. Synooka, K.-R. Eberhardt, C. R. Singh, F. Hermann, G. Ecke, B. Ecker, E. von Hauff, G. Gobsch, and H. Hoppe, *Adv. Energy Mater.* **4**, 1300981 (2014).
- 36) E. Verploegen, R. Mondal, C. J. Bettinger, S. Sok, M. F. Toney, and Z. Bao, *Adv. Funct. Mater.* **20**, 3519 (2010).
- 37) M. S. Ryu, H. J. Cha, and J. Jang, *Curr. Appl. Phys.* **10**, S206 (2010).
- 38) M. M. Tavakoli, L. Gu, Y. Gao, C. Reckmeier, J. He, A. L. Rogach, Y. Yao, and Z. Fan, *Sci. Rep.* **5**, 14083 (2015).
- 39) Q. Chen, H. Zhou, Z. Hong, S. Luo, H.-S. Duan, H.-H. Wang, Y. Liu, G. Li, and Y. Yang, *J. Am. Chem. Soc.* **136**, 622 (2014).

- 40) Y. Deng, E. Peng, Y. Shao, Z. Xiao, Q. Dong, and J. Huang, *Energy Environ. Sci.* **8**, 1544 (2015).

Figure Captions

Fig. 1. (Color online) TEM cross-sectional image of the selected AZO (50 nm)/Ag (13 nm)/AZO (50 nm) sample.

Fig. 2. (Color online) RBS measurement results for (a) AZO/Ag/AZO multilayer and (b) single-layer AZO structures on glass substrates. Open squares indicate the experimental data, while solid lines the fitted data.

Fig. 3. (Color online) (a) Spectral transmittance, (b) reflectance, and (c) absorbance of AZO/Ag/AZO sandwich structures with different Ag interlayer layer thicknesses and single-layer AZO (50 nm) as the reference sample.

Fig. 4. (Color online) XRD patterns of AZO/Ag/AZO multilayer sandwich structures with different Ag interlayer thicknesses. (Δ) for the ZnO peak and (\bullet) for the Ag peak.

Fig. 5. (Color online) SEM (top row) and AFM (bottom row) images of AZO/Ag/AZO multilayer sandwich structures with different Ag interlayer thicknesses.

Fig. 6. (Color online) Variations in effective carrier concentration, mobility and film resistivity of the multilayer sandwich structures as a function of AZO top layer thickness.

Fig. 7. (Color online) (a) Spectral transmittance, (b) reflectance, and (c) absorbance of AZO/Ag/AZO sandwich structures with different AZO top layer thicknesses.

Fig. 8. (Color online) Photographs of three AZO/Ag/AZO samples deposited using different types of Ar-diluted O₂ gas after the tape test.

Fig. 9. (Color online) XRD peaks of AZO/Ag/AZO films deposited using low or high O₂ partial pressure.

Fig. 10. (Color online) Variations in effective carrier concentration, mobility, and film resistivity of the multilayer sandwich structures as a function of annealing temperature for (a) 5 min annealing, and (b) 10 min annealing.

Table I. Sputter deposition conditions for each layer of the AZO/Ag/AZO multilayer sandwich structures investigated.

Process parameters	AZO (bottom)	Ag	AZO (top)
Target type	dual cylindrical ceramic	planar metallic	dual cylindrical ceramic
Substrate temperature (°C)	~200	RT	~200
Preheating pass	6	–	0
Pressure (mbar)	3×10^{-3}	3×10^{-3}	3×10^{-3}
Power source	Pulsed DC	DC	Pulsed DC
Power (kW)	2.0	0.6 / 0.5	2.0
Ar flow rate (sccm)	205	120	205
Film thickness (nm)	50	10 / 13 / 16	20 – 100
Substrate	3-mm-thick soda-lime glass		

Table II. Electrical properties of the AZO/Ag/AZO multilayer sandwich structures and single-layer AZO (50 nm).

	Ag thickness (nm)	R_{sh} (Ω /sq)	Resistivity (Ω cm)	Concentra- tion (cm^{-3})	Mobility ($\text{cm}^2\text{V}^{-1}\text{s}^{-1}$)
AZO/	10	10.9	1.2×10^{-4}	5.3×10^{21}	10.3
Ag/	13	5.7	6.4×10^{-5}	8.5×10^{21}	11.7
AZO	16	3.4	3.9×10^{-5}	1.2×10^{22}	12.3
Single-layer AZO (50 nm)	–	1706	8.5×10^{-3}	1.5×10^{20}	4.9

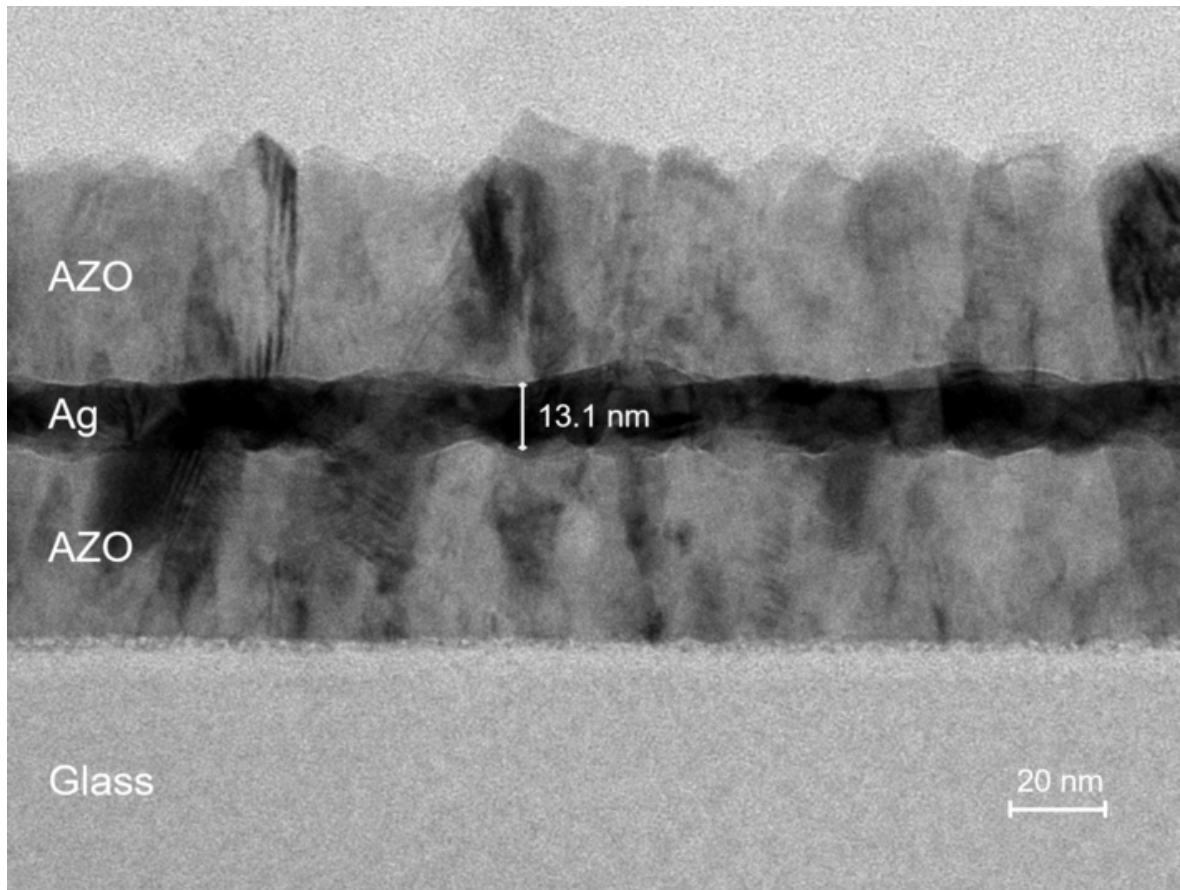


Fig. 1. (Color online)

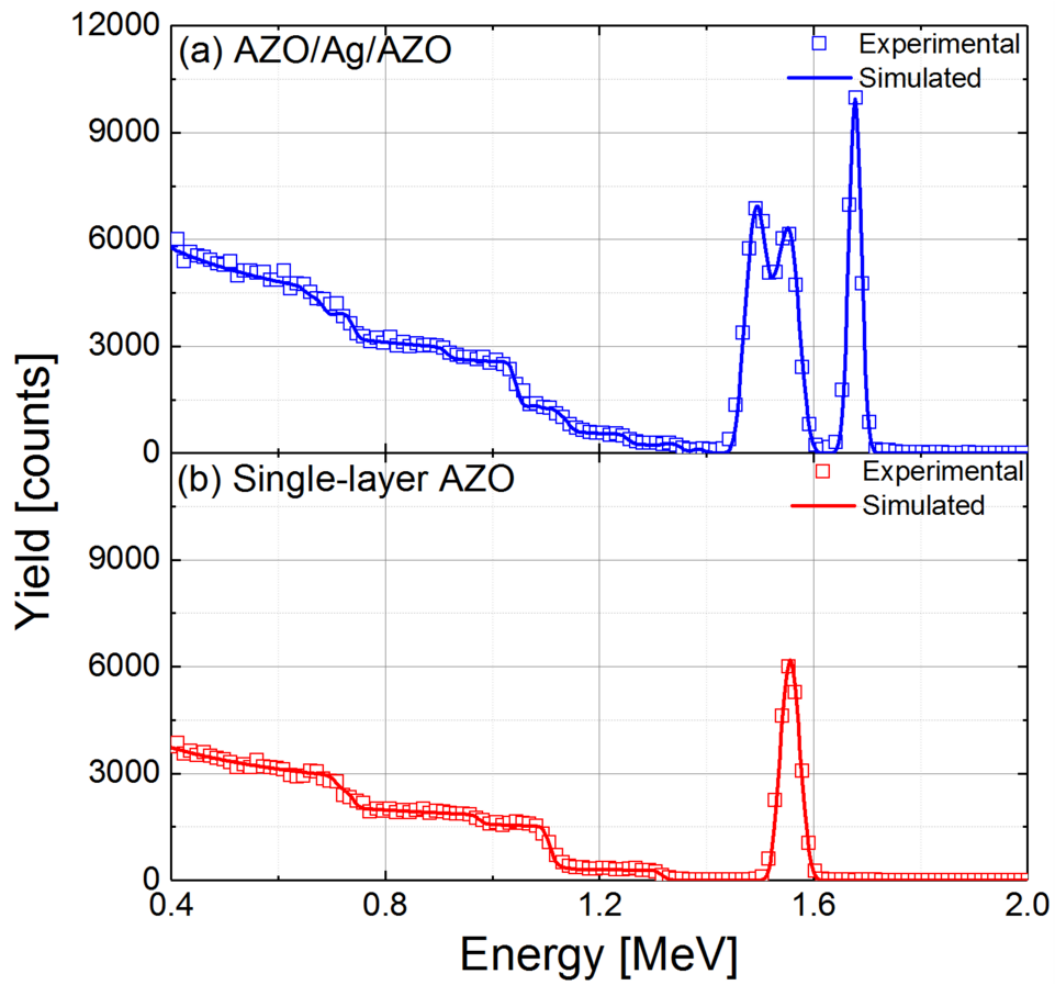


Fig. 2. (Color online)

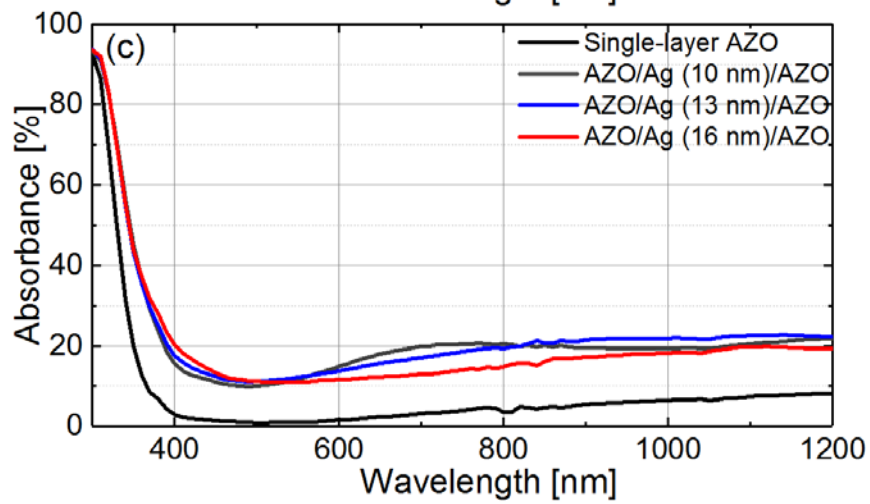
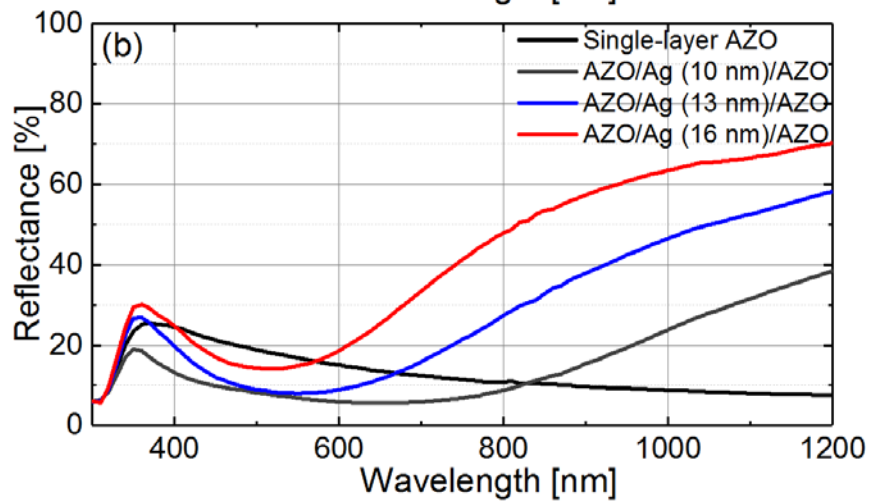
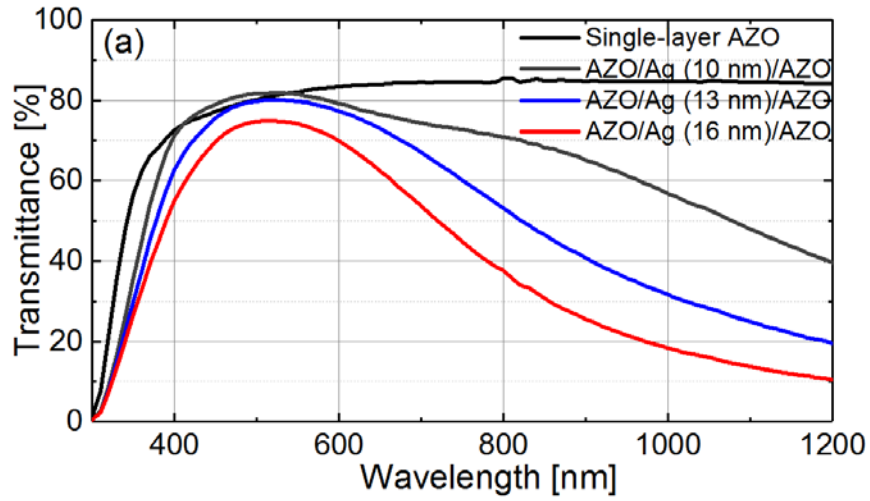


Fig. 3. (Color online)

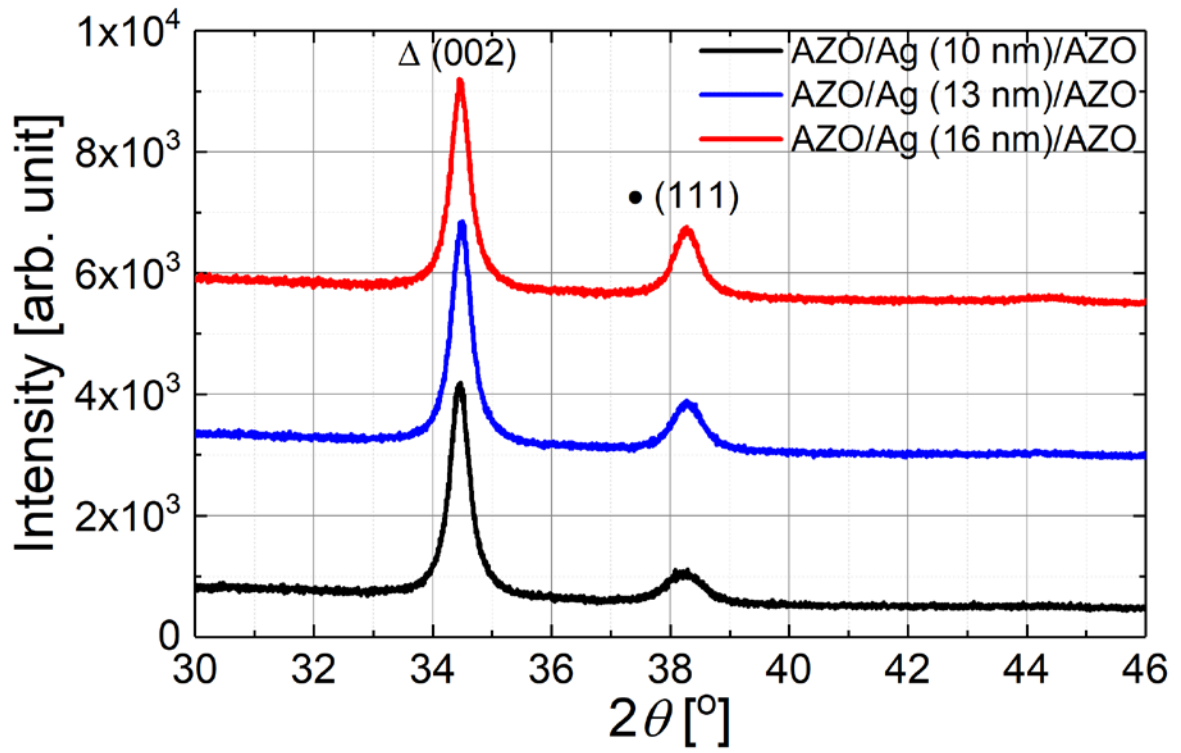


Fig. 4. (Color online)

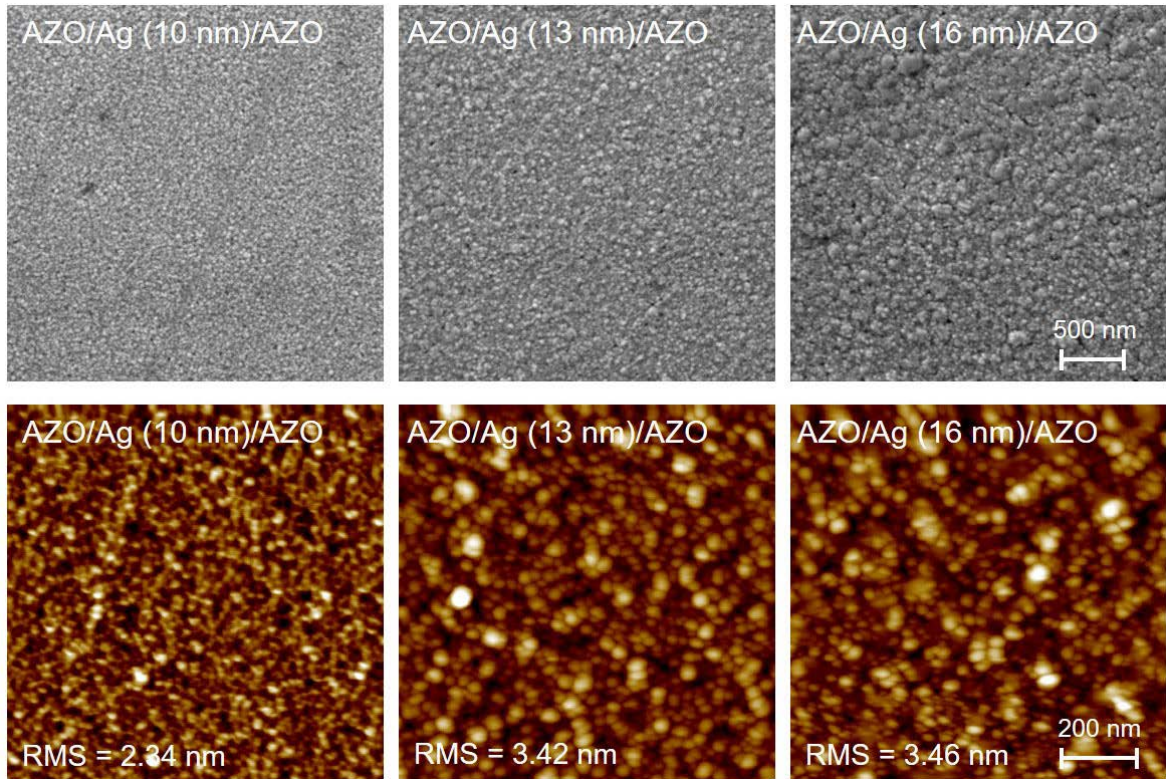


Fig. 5. (Color online)

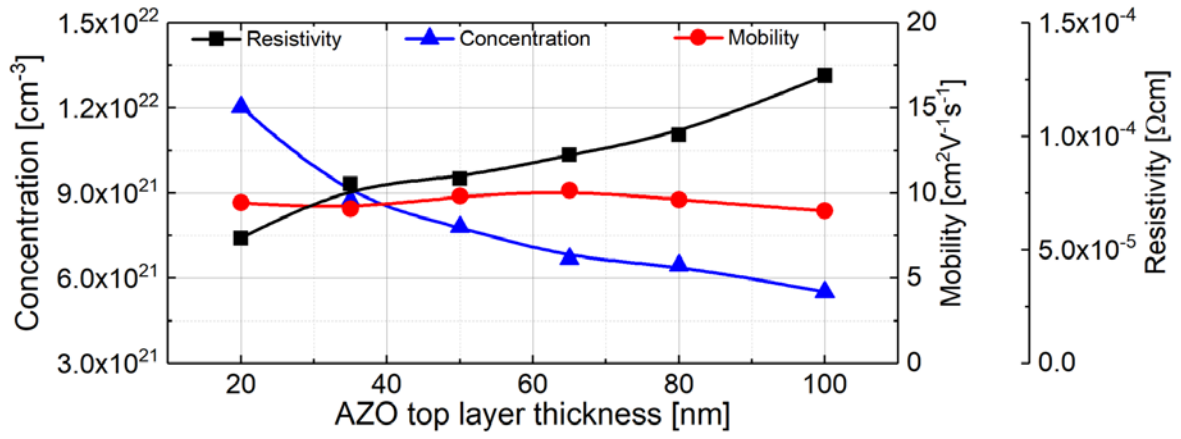


Fig. 6. (Color online)

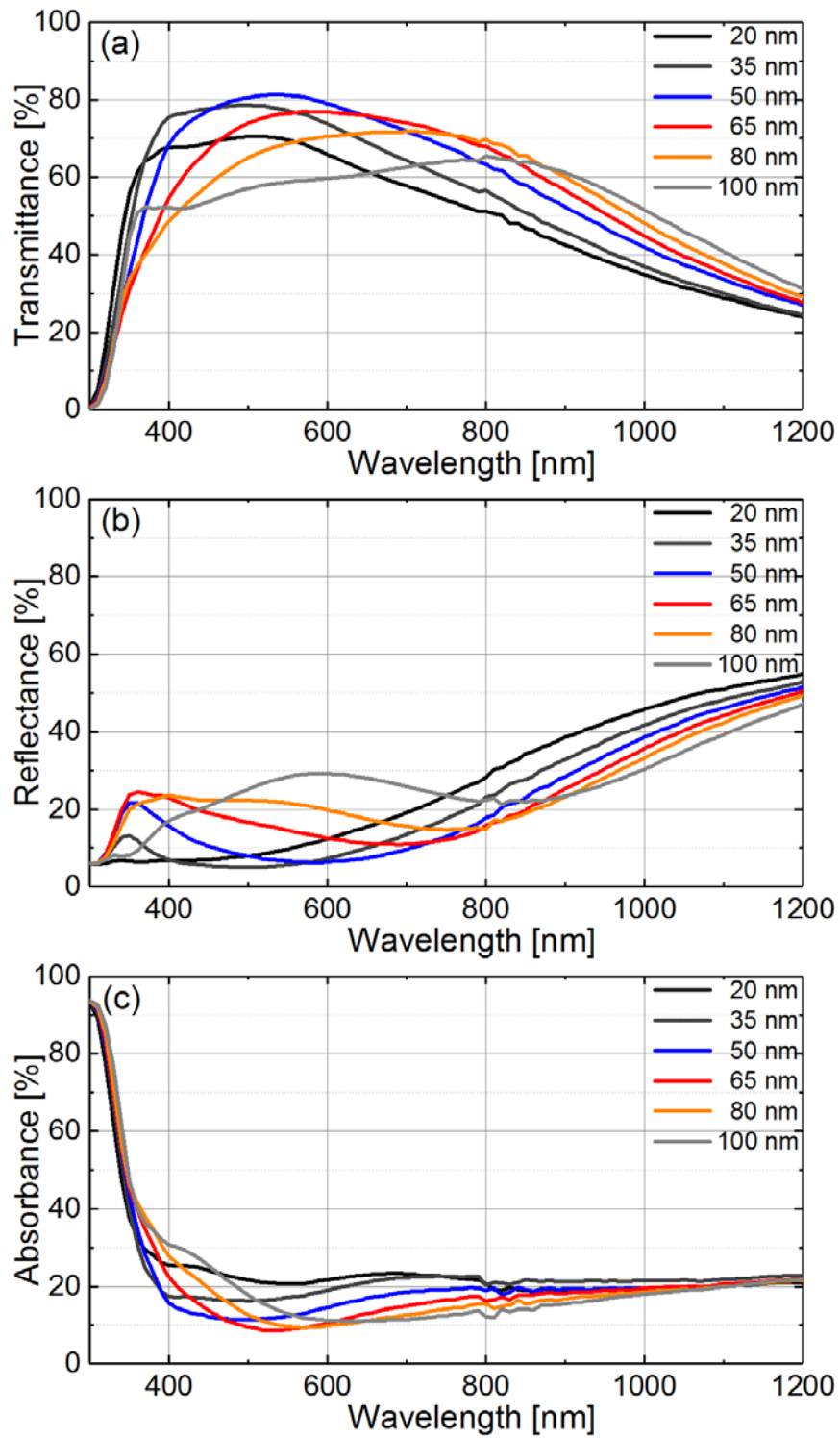


Fig. 7. (Color online)

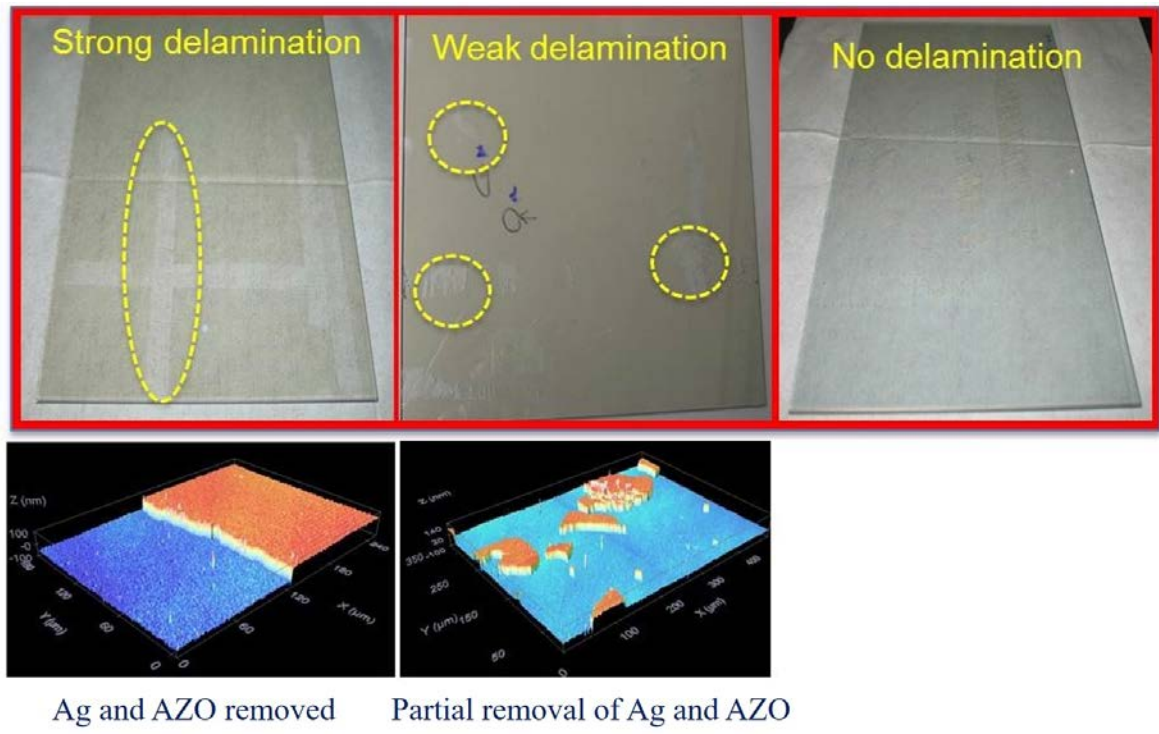


Fig. 8. (Color online)

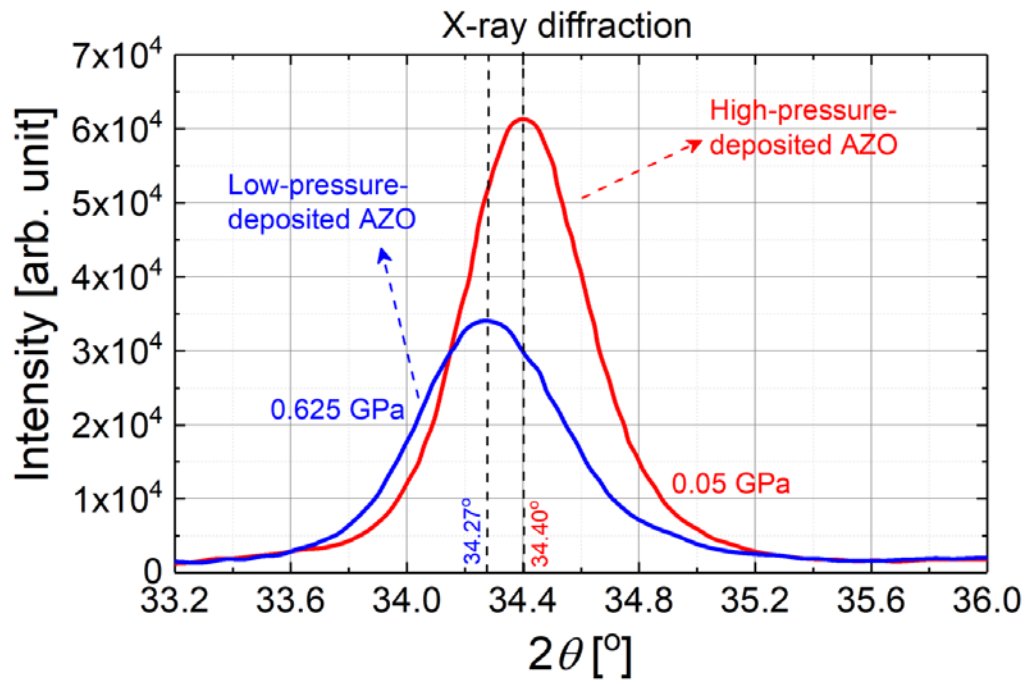


Fig. 9. (Color online)

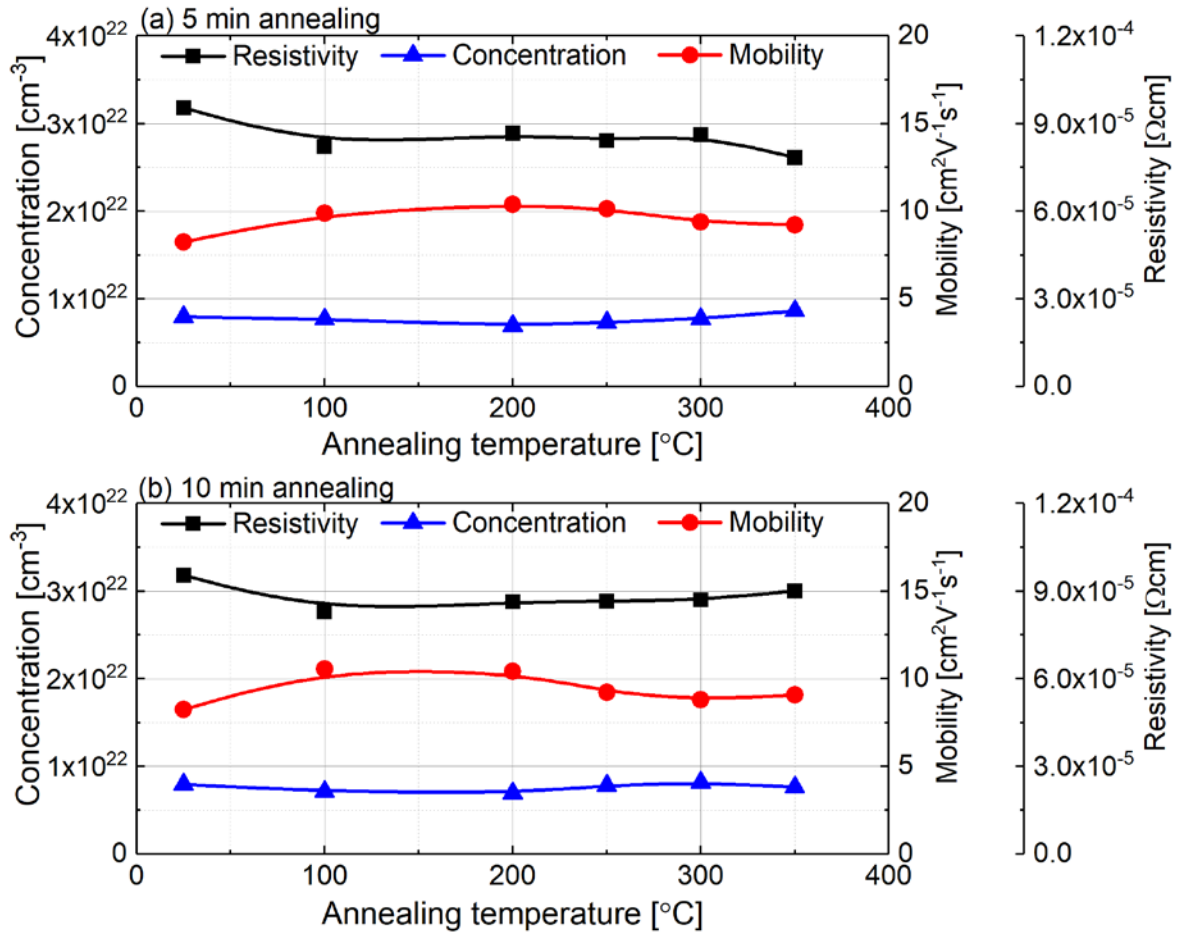


Fig. 10. (Color online)